# Nonlinear analysis of the deformation and breakup of viscous microjets using the method of lines

E. P. Furlani[1, *, †] and M. S. Hanchak[2]

[1]*Research Laboratories, Eastman Kodak Company, 1999 Lake Avenue, Rochester, NY 14650-2216, U.S.A.*
[2]*Graphic Communications Group, Eastman Kodak Company, 3000 Research Blvd, Dayton, OH 45420, U.S.A.*

## SUMMARY

We present a numerical model for predicting the instability and breakup of viscous microjets of Newtonian fluid. We adopt a one-dimensional slender-jet approximation and obtain the equations of motion in the form of a pair of coupled nonlinear partial differential equations (PDEs). We solve these equations using the method of lines, wherein the PDEs are transformed to a system of ordinary differential equations for the nodal values of the jet variables on a uniform staggered grid. We use the model to predict the instability and satellite formation in infinite microthreads of fluid and continuous microjets that emanate from an orifice. For the microthread analysis, we take into account arbitrary initial perturbations of the free-surface and jet velocity, as well as Marangoni instability that is due to an arbitrary variation in the surface tension. For the continuous nozzle-driven jet analysis, we take into account arbitrary time-dependent perturbations of the free-surface, velocity and/or surface tension as boundary conditions at the nozzle orifice. We validate the model using established computational data, as well as axisymmetric, volume of fluid (VOF) computational fluid dynamic (CFD) simulations. The key advantages of the model are its ease of implementation and speed of computation, which is several orders of magnitude faster than the VOF CFD simulations. The model enables rapid parametric analysis of jet breakup and satellite formation as a function of jet dimensions, modulation parameters, and fluid rheology. Copyright © 2010 John Wiley & Sons, Ltd.

## 1. INTRODUCTION

The instability of slender liquid jets has been the subject of countless research articles dating back to 1833 with experimental work by Savart [1]. In 1849, Plateau was the first to postulate that surface tension was the cause of jet breakup [2]. However, it was not until 1879 that Lord Rayleigh put this hypothesis on solid theoretical ground [3]. Rayleigh considered the behavior of an infinite, stationary liquid cylinder in a vacuum, with an initial infinitesimal sinusoidal displacement of wavelength $\lambda$ imposed along the free-surface. He obtained a dispersion relation for the disturbance growth rate as a function of the wavenumber ($k = 2\pi/\lambda$), and found that the fastest growing disturbance occurs when $\lambda \approx 4.5D$ (diameter). Following Rayleigh, there has been a sustained and growing interest in jet instability, as this process plays a critical role in a wide range of fundamental phenomena with practical applications spanning multiple disciplines and length scales [4]. A comprehensive overview of this topic has recently been given by Eggers and Villermaux [5].

*Correspondence to: E. P. Furlani, Research Laboratories, Eastman Kodak Company, 1999 Lake Avenue, Rochester, NY 14650-2216, U.S.A.
†E-mail: edward.furlani@kodak.com
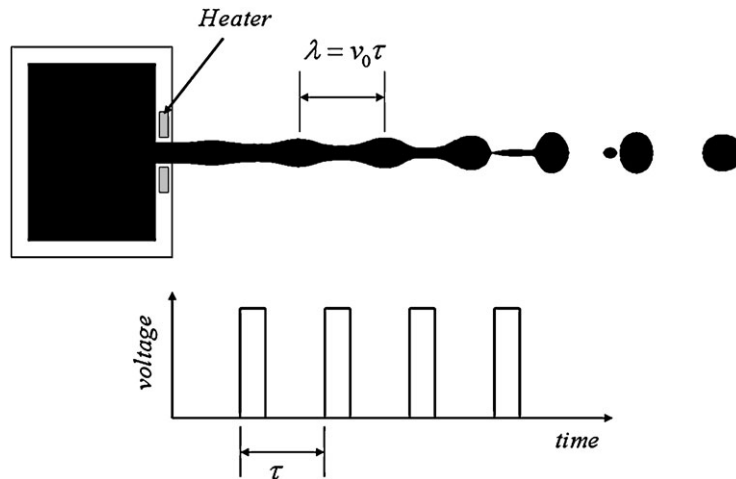
Figure 1. Illustration showing a single nozzle with an integrated heater at the orifice, and a thermal modulation pulse used to induce Marangoni instability and drop formation.

Research into the phenomenon of jet breakup and drop formation has increased dramatically over the last several years, due in part to the rapid advances in microfluidic, biomedical and nanoscale technologies. Novel applications are proliferating, especially in fields that benefit from high-speed and low-cost patterned deposition of discrete samples (droplets) of micro- or nanoscale materials. A wide range of materials can potentially be jetted using modern microfluidic devices including liquid metals, dispersions of nanoparticles, electrical, and optical polymers, myriad biomaterials, sealants and adhesives. Emerging applications in this field include printing functional materials for flexible electronics, microdispensing of biochemicals, printing biomaterials (e.g. cells, genetic material), and 3D rapid prototyping [6–11].

The most notable and commercially successful application in this field is the traditional inkjet printing wherein droplets of ink are generated at high repetition rates and directed onto a media to render an image. Recently, novel integrated microfluidic inkjet devices have been developed that utilize thermally modulated jets to enable color printing with unprecedented speed and versatility [12–15]. These devices consist of a pressurized reservoir that feeds a microfluidic nozzle manifold with hundreds of active orifices, each of which produces a continuous microjet of fluid. The controlled thermal modulation of each jet is achieved using CMOS/MEMS technology wherein a resistive heater element is integrated into the nozzle surrounding each orifice. To modulate a jet, a periodic voltage is applied to the heater, which causes a periodic diffusion of thermal energy from the heater into the fluid near the orifice (Figure 1). Thus, the temperature of fluid, and hence the temperature-dependent fluid properties, density, viscosity and surface tension, are modulated near the orifice. The dominant cause of jet instability is the modulation of surface tension. In the first order, the temperature dependence of $\sigma$ is given by $\sigma(T) = \sigma_0 - \beta(T - T_0)$, where $\sigma(T)$ and $\sigma_0$ are the surface tension at temperatures $T$ and $T_0$, respectively. The pulsed heating modulates $\sigma$ at a wavelength $\lambda = v_0\tau$, where $v_0$ is the jet velocity and $\tau$ is the period of the heat pulse as shown in Figure 1. The downstream advection of thermal energy gives rise to a spatial variation (gradient) of surface tension along the jet. This produces a shear stress at the free-surface, which is balanced by inertial forces in the fluid, thereby inducing a Marangoni flow towards regions of higher surface tension (from warmer regions towards cooler regions). This causes a deformation of the free-surface (slight necking in the warmer regions and ballooning in the cooler regions) that ultimately leads to instability and drop formation [13]. The drop volume can be adjusted on demand by varying $\tau$, i.e. $V_{\text{drop}} = \pi r_0^2 v_o \tau$. Thus, longer pulses produce larger drops, shorter pulses produce smaller drops and different sized drops can be produced from each orifice as desired.

The development of reliable high-throughput microscale droplet-generating devices requires considerable fluidic modeling in advance of device fabrication. Such modeling is essential in order

to obtain sufficient understanding of jetting and drop generation to enable device optimization taking into account critical system parameters as well as the fluid rheology. A rigorous analysis of microfluidic drop generators requires multiphase free-surface computational fluid dynamic (CFD) simulations, often with coupled thermal and structural analysis. While various numerical techniques have been developed for simulating free-surface flows, each has advantages and drawbacks, and all such methods tend to be computationally intensive. The computational methods can be broadly classified as Lagrangian or Eulerian, or hybrid combinations of the two [16–21]. In Lagrangian methods, the fluid interface is tracked with computational nodes that move with the fluid velocity. While this provides an accurate description of the free-surface, its main disadvantage is that the mesh can become severely distorted over time, and the careful monitoring of mesh quality is required with frequent remeshing that significantly adds to the computational overhead. Arbitrary Lagrangian–Eulerian methods can remedy this problem by allowing the nodes to move independent of the fluid velocity thereby maintaining mesh quality and minimizing remeshing, but implementation can be nontrivial for complex flows. In the Eulerian approach, the computational mesh is fixed, and an unknown function is introduced and solved for whose values define the volume fraction of fluid in each computational cell. The most common implementation of this approach is the volume of fluid (VOF) method [22]. While VOF has advantages in terms of implementation and computational speed, its main disadvantage is that the free-surface is reconstructed via interpolation, which gives rise to errors in surface curvature and hence the fluid pressure. Other methods finding increasing use for free-surface analysis include the level set and phase field techniques [23, 24].

As an alternative or supplement to computationally intensive CFD analysis, one can simplify the problem and study the dynamics of the jet instability and drop formation using a simplified 1D slender-jet analysis. In the slender-jet approximation, the free-surface is represented by a shape function $h(z, t)$, where $z$ is the axial coordinate and $t$ is time. The Navier–Stokes (NS) equations, mass conservation and appropriate boundary conditions (BCs) are simplified and combined to obtain coupled partial differential equations (PDEs) that govern the fluid velocity $v(z, t)$ along the jet, and free-surface function $h(z, t)$ [25]. Various methods have been used to solve the slender-jet equations. Eggers and Dupont [25] and Brenner *et al.* [26] used a finite difference approach with a nonuniform, graded spatial mesh that was adaptively refined, and an adaptive fully implicit $\theta$-weighted time-integration scheme. Ambravaneswaran *et al.* used the Galerkin finite element method for the spatial discretization, and an adaptive, implicit finite difference method for time discretization [23]. It has been found that 1D analysis can provide reasonably accurate predictions of jet breakup for a range of practical applications [25–27]. Moreover, 1D models are relatively easy to implement and modify, and can reduce the simulation time by orders of magnitude relative to axisymmetric CFD analysis.

In this paper, we develop a 1D slender-jet model to predict the nonlinear deformation and breakup of infinite microthreads and continuous nozzle-driven jets of the Newtonian fluid. We take into account the Marangoni instability by allowing for a variation in surface tension in our derivation of the equations of motion. The slender-jet equations reduce to a pair of coupled PDEs for the free-surface $h$ and velocity $v$ of the jet. We solve these equations using the method of lines (MOL), wherein the PDEs are transformed to a system of ordinary differential equations (ODEs) that define the behavior of $h$ and $v$ at the nodes of a uniform staggered computational grid. We integrate the ODE system using explicit forward time-stepping, and track the behavior of the free-surface and the velocity to pinch-off. A key advantage of the MOL approach is that it enables the use of well-established and robust numerical methods for solving the coupled ODEs. The use of explicit time stepping and a fixed uniform spatial grid provides additional advantages in that they facilitate implementation of the model with less complexity than other numerical approaches.

We demonstrate the model via application to practical examples, and characterize its accuracy using both established computational data from the literature as well as axisymmetric VOF CFD simulations. In this regard, while other authors have used slender-jet analysis to study jet breakup, relatively few have compared their predictions with independent VOF CFD simulations. We choose VOF CFD to test our model because of its availability in commercial fluid simulators, i.e. it is the most commonly implemented approach for free-surface analysis.

We first study the breakup of microthreads of fluid and show that a typical analysis can be completed within a few seconds on a modern workstation. This is four orders of magnitude faster than the corresponding VOF CFD simulations. Moreover, it is important to note that while it is easy to impose initial perturbations to a fluid microthread in our model, it can be very difficult to impose such perturbations, especially infinitesimal free-surface displacements, using the VOF CFD approach.

We perform similar analysis of a continuous nozzle-driven jet wherein the jet disturbance is imposed as a time-dependent BC at the nozzle orifice. We show that jet instability and pinch-off predictions require a few minutes to complete, which is between one and two orders faster than VOF CFD simulations. Again, not only is the analysis faster, but the time-dependent BCs are much easier to implement in our model as compared with the VOF CFD analysis.

## 2. THEORY

In this section we derive the equations of motion for an isothermal axisymmetric viscous microjet of incompressible Newtonian fluid with surface tension $\sigma$, viscosity $\mu$ and density $\rho$. We neglect gravity, and take into account Marangoni instability by allowing for a spatial variation of surface tension along the jet. We solve the following equations:

*Navier–Stokes:*

$$\rho \frac{\mathrm{D}v}{\mathrm{D}t} = -\nabla p + \mu \nabla^2 v, \tag{1}$$

where $\mathrm{D}/\mathrm{D}t = \partial/\partial t + v \cdot \nabla$.

*Continuity:*

$$\nabla \cdot v = 0. \tag{2}$$

### 2.1. Boundary conditions

The BCs for this problem include stress balance, a kinematic condition, and axisymmetric flow conditions. The first two conditions apply at the free-surface (liquid–gas interface), while the flow conditions apply along the axis of the microjet. The stress balance at the free-surface can be written as

$$\hat{n} \cdot \mathbb{T} = -2H\sigma\hat{n} + \nabla_s \sigma, \tag{3}$$

where $\mathbb{T}$ is the stress tensor in the fluid (we assume that the external gas is stress free),

$$H = \frac{1}{2}\left(\frac{1}{h(1+h'^2)^{1/2}} - \frac{h''}{(1+h'^2)^{3/2}}\right), \tag{4}$$

and $\hat{n}$ and $\hat{t}$ are unit vectors normal and tangential to the free-surface (Figure 2),

$$\hat{n} = \hat{r}\frac{1}{\sqrt{1+h'^2}} - \hat{z}\frac{h'}{\sqrt{1+h'^2}}, \tag{5}$$
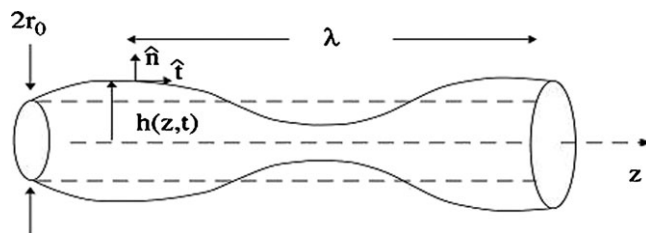


Figure 2. Slender jet geometry and reference frame.

$$\hat{t} = \hat{r}\frac{h'}{\sqrt{1+h'^2}} + \hat{z}\frac{1}{\sqrt{1+h'^2}}. \tag{6}$$

The surface gradient $\nabla_s$ is

$$\nabla_s = \hat{r}\frac{h'}{(1+h'^2)}\frac{\partial}{\partial z} + \hat{z}\frac{1}{(1+h'^2)}\frac{\partial}{\partial z}. \tag{7}$$

In these expressions $h(z,t)$ defines the radial position of the free-surface, and $h' = \partial h/\partial z$.

Equation (3) can be decomposed into normal and tangential components:

$$(\hat{n} \cdot \mathbb{T}) \cdot \hat{n} = -2H\sigma \quad \text{(normal stress)} \tag{8}$$

$$(\mathbb{T} \cdot \hat{n}) \cdot \hat{t} = \hat{t} \cdot \nabla_s \sigma \quad \text{(tangential stress)} \tag{9}$$

where

$$\hat{t} \cdot \nabla_s \sigma = \frac{1}{\sqrt{1+h'^2}}\frac{\partial \sigma}{\partial z}. \tag{10}$$

The gradient of surface tension $\nabla_s \sigma$ produces a Marangoni flow towards regions of higher surface tension, which deforms the free-surface and ultimately causes breakup [13].

The second (kinematic) BC implies that fluid does not cross the free-surface,

$$\frac{\mathrm{D}}{\mathrm{D}t}(r - h(z,t)) = 0 \quad (r = h). \tag{11}$$

The flow conditions along the axis of the jet ($r = 0$) are

$$v_r = 0, \tag{12}$$

and

$$\frac{\partial v_z}{\partial r} = 0, \tag{13}$$

## 2.2. Solution method

Our solution method is based on a perturbation analysis described by Eggers and Dupont in which the jet variables are expanded in power series of the radial variable $r$ [25]. First, we write all equations and BCs in component form. For axisymmetric flow, the NS equation (1) reduces to,

$$\rho\left(\frac{\partial v_r}{\partial t} + v_r\frac{\partial v_r}{\partial r} + v_z\frac{\partial v_r}{\partial z}\right) = -\frac{\partial p}{\partial r} + \mu\left[\frac{\partial}{\partial r}\left(\frac{1}{r}\frac{\partial(rv_r)}{\partial r}\right) + \frac{\partial^2 v_r}{\partial z^2}\right], \tag{14}$$

and

$$\rho\left(\frac{\partial v_z}{\partial t} + v_r\frac{\partial v_z}{\partial r} + v_z\frac{\partial v_z}{\partial z}\right) = -\frac{\partial p}{\partial z} + \mu\left[\frac{1}{r}\frac{\partial}{\partial r}\left(r\frac{\partial v_z}{\partial r}\right) + \frac{\partial^2 v_z}{\partial z^2}\right]. \tag{15}$$

The continuity condition (2) becomes

$$\frac{1}{r}\frac{\partial(rv_r)}{\partial r} + \frac{\partial v_z}{\partial z} = 0. \tag{16}$$

The normal and tangential stress BCs (8) and (9) can be written as

$$p + \frac{2\mu}{(1+h'^2)}\left[h'\left(\frac{\partial v_z}{\partial r} + \frac{\partial v_r}{\partial z}\right) - \frac{\partial v_r}{\partial r} - h'^2\frac{\partial v_z}{\partial z}\right] = -\sigma\left[\frac{1}{h(1+h'^2)^{1/2}} - \frac{h''}{(1+h'^2)^{3/2}}\right]$$

$$(r = h) \tag{17}$$

and

$$\frac{\mu}{(1+h'^2)}\left[2h'\left(\frac{\partial v_r}{\partial r}-\frac{\partial v_z}{\partial z}\right)+(1-h'^2)\left(\frac{\partial v_r}{\partial z}+\frac{\partial v_z}{\partial r}\right)\right]=\frac{1}{\sqrt{1+h'^2}}\frac{\partial \sigma}{\partial z} \quad (r=h). \tag{18}$$

Similarly, the kinematic condition (11) gives

$$\frac{\partial h}{\partial t}+v_z h'=v_r \quad (r=h). \tag{19}$$

We seek a solution to Equations (14)–(19). To this end, we expand $v_z(r,z,t)$ and $p(r,z,t)$ in powers of $r$ [21]

$$v_z(r,z,t)=v_0(z,t)+v_2(z,t)r^2+\cdots, \tag{20}$$

$$p(r,z,t)=p_0(z,t)+p_2(z,t)r^2+\cdots. \tag{21}$$

From the continuity condition (16) and the expansion (20) we obtain

$$v_r(r,z,t)=-\frac{\partial v_0(z,t)}{\partial z}\frac{r}{2}-\frac{\partial v_2(z,t)}{\partial z}\frac{r^3}{4}+\cdots \tag{22}$$

Notice that these expansions are compatible with the BCs (12) and (13).

Using expansions (20)–(22) we find that the equation of motion (14) for $v_r$ is identically satisfied to lowest order. However, Equation (15) for $v_z$ gives

$$\frac{\partial v_0}{\partial t}+v_0\frac{\partial v_0}{\partial z}=-\frac{1}{\rho}\frac{\partial p_0}{\partial z}+\frac{\mu}{\rho}\left(4v_2+\frac{\partial^2 v_0}{\partial z^2}\right). \tag{23}$$

To solve for $v_0$ we need to eliminate the second-order term $v_2$ from (23). To this end, we evaluate the tangential stress condition (18) at $r=h$, collect lowest-order terms, and obtain,

$$v_2=\frac{1}{2\mu h}\frac{\partial \sigma}{\partial z}+\frac{3}{2h}\frac{\partial h}{\partial z}\frac{\partial v_0}{\partial z}+\frac{1}{4}\frac{\partial^2 v_0}{\partial z^2}. \tag{24}$$

Furthermore, from the normal stress BC (17) we find that

$$p_0=-\mu\frac{\partial v_0}{\partial z}+2\sigma H. \tag{25}$$

We substitute (24) and (25) into (23) and obtain

$$\frac{\partial v_0}{\partial t}=-v_0\frac{\partial v_0}{\partial z}-\frac{1}{\rho}\frac{\partial}{\partial z}(2\sigma H)+\frac{2}{\rho h}\frac{\partial \sigma}{\partial z}+\frac{3\mu}{\rho h^2}\frac{\partial}{\partial z}\left(h^2\frac{\partial v_0}{\partial z}\right). \tag{26}$$

Finally, the kinematic condition (19) can be rewritten as:

$$\frac{\partial(h^2)}{\partial t}=-\frac{\partial(h^2 v_0)}{\partial z}, \tag{27}$$

Which is a statement of the conservation of volume applied to a cylindrical slice of the jet. We solve the slender-jet equations (26) and (27) subject to appropriate BCs using the MOL [28]. Specifically, we define a uniform staggered grid along the jet and write the spatial derivatives as finite differences with respect to this grid. The partial time derivatives of the variables $v_0$ and $h$ become ordinary time derivatives of the respective nodal values. We evaluate $h$ and $p$ on one set of nodes, and $v_0$ on a different set of interlaced nodes as shown in Figure 3. Thus, for example, Equation (27) reduces to a system of $N$ ODEs of the form

$$\frac{\partial h_i}{\partial t}=-\frac{h_{i+1/2}^2 v_i-h_{i-1/2}^2 v_{i-1}}{2h_i\Delta z} \quad (1\leqslant i\leqslant N), \tag{28}$$
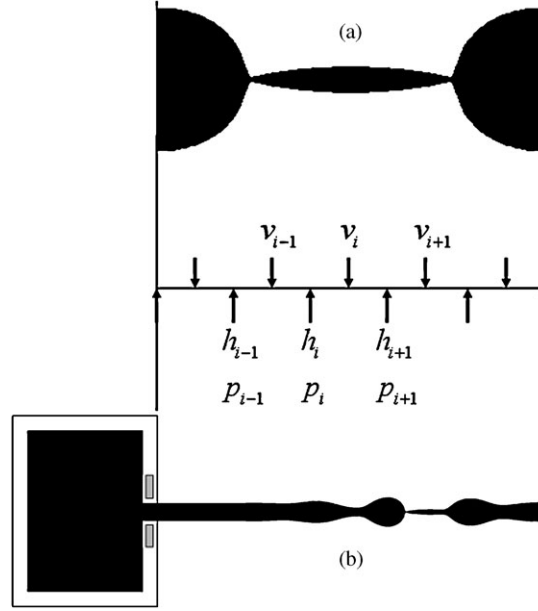
Figure 3. Staggered computational grid: (a) infinite cylinder at pinch-off with periodic BCs and (b) nozzle-driven microjet.

where $N$ is the number of nodes, and $h_{i+1/2} = \frac{1}{2}(h_i + h_{i+1})$, $h_{i-1/2} = \frac{1}{2}(h_i + h_{i-1})$. A similar system of ODEs is obtained for Equation (26), and therefore a total of $2N$ ODEs need to be solved for each simulation. We apply a numerical upwind differencing scheme for the advection term in Equation (26) and forward or central differencing for the remaining terms.

We have implemented the MOL in MATLAB using the ODE solver routines for our numerical studies. MATLAB provides several different ODE solvers; they differ in order of accuracy and robustness to stiff equations. We investigated the performance of various solvers and ultimately chose the ode23t solver, which employs the trapezoidal integration rule using a 'free' interpolant. This solver provided the fastest solution times with adequate accuracy. We developed models to study both infinite *microthreads* of fluid with arbitrary modulation of the free-surface or surface tension along the jet, and nozzle-driven microjets, wherein the modulation is applied in a time-wise fashion at the orifice, and then convected downstream.

## 3. RESULTS

In this section we demonstrate the model via application to both an infinite microthread of the Newtonian fluid as well as a continuous nozzle-driven microjet. We validate the model using the established data from the literature as well as VOF CFD simulations. In order to consistently compare our results, we scale the equations of motion using characteristic values for velocity, length and time. The velocity is scaled by the capillary velocity, which is given by:

$$v_c = \sqrt{\frac{\sigma}{\rho r_0}}. \tag{29}$$

The most appropriate length scale is the initial jet radius, $r_0$. Hence, the time scale is determined by dividing the length scale by the velocity scale,

$$t_c = \sqrt{\frac{\rho r_0^3}{\sigma}}. \tag{30}$$

In our analysis below, we present our results using a scaled time $t^* = t/t_c$, where $t$ is the physical time. Since the temporal analysis in this paper essentially models a stationary microthread of fluid, the Reynolds number based on velocity has no immediate meaning. Hence, we substitute the capillary velocity into the familiar Reynolds number equation to achieve a temporal Reynolds number that is also the inverse of the Ohnesorge number,

$$Re = \frac{\rho v_c r_0}{\mu} = \frac{\sqrt{\rho \sigma r_0}}{\mu}. \tag{31}$$

Thus, for example, given the density, surface tension and initial jet radius, the Reynolds number precisely determines the viscosity. The nominal fluid properties used in our analyses are those of water at standard temperature and pressure, $\rho = 998 \, \text{kg/m}^3$, $\sigma = 0.073 \, \text{N/m}$ and $\mu = 0.001 \, \text{N s/m}^2$.

We begin our study with an analysis of an infinite micro-thread of Newtonian fluid. While we could easily impose an arbitrary initial perturbation to the free-surface, velocity or surface tension along the thread, for simplicity, we choose a sinusoidal perturbation of the free-surface,

$$h(z, 0) = r_0 \left( 1 + \varepsilon \cos \left( \frac{2\pi z}{\lambda} \right) \right), \tag{32}$$

where $\lambda$ is the wavelength. The initial perturbation has a peak amplitude equal to 5% of unperturbed jet radius, i.e. $\varepsilon = 0.05$. For our test cases we use data published by Ashgriz and Mashayek, who used a Galerkin finite element method to study the instability of an axisymmetric, incompressible Newtonian liquid cylinder [4]. They employed a moving mesh, which required time-dependent shape functions to capture the surface deformation.

We set the jet radius to $r_0 = 100 \, \mu\text{m}$ and model the following parameters: $Re = 200$, $k = 0.7$; $Re = 200$, $k = 0.45$; $Re = 0.1$, $k = 0.45$; and $Re = 0.1$, $k = 0.7$, where $k = 2\pi r_0/\lambda$ is the wavenumber scaled by the initial jet radius. For the remainder of the paper, we refer specifically to this scaled wavenumber. Some typical free-surface plots at pinch-off are shown in Figure 4. The number of grid points for this analysis ranged from 135 for $k = 0.7$ to 210 for $k = 0.45$, and the corresponding computational time ranged from 4 to 12 s using a single processor workstation. Our predictions of the scaled time, $t^* = t/t_c$, are compared with those obtained by Ashgriz and Mashayek in Table I. Note that our 1D model provides excellent agreement with the FEA-based predictions for all but
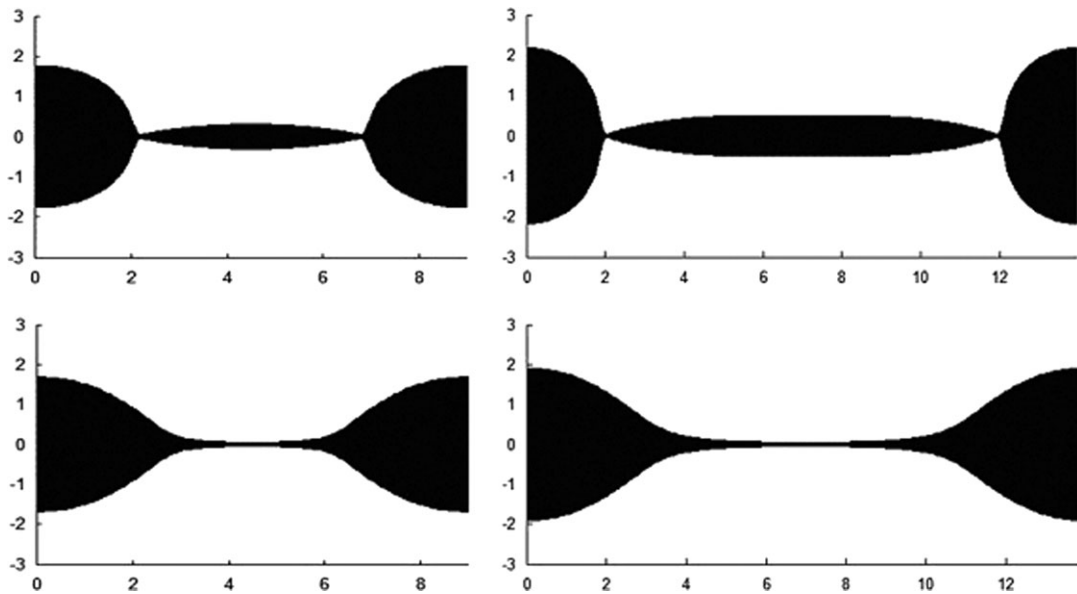


Figure 4. The shape of the free-surface at pinch-off (clock-wise from top left): $Re = 200$, $k = 0.7$; $Re = 200$, $k = 0.45$; $Re = 0.1$, $k = 0.45$; $Re = 0.1$, $k = 0.7$.

Table I. A comparison of scaled break-up times from the 1D model (bold font) with the model of Ashgriz and Mashayek (regular font) [24].

| Reynolds Number | Wavenumber | | | |
|---|---|---|---|---|
| | 0.2 | 0.45 | 0.7 | 0.9 |
| 200 | 25.2 | 12.9 | 10.0 | 14.5 |
| | **25.0** | **12.6** | **9.7** | **11.0** |
| 10 | 26.7 | 14.3 | 11.6 | 14.8 |
| | **27.9** | **14.3** | **11.4** | **14.4** |
| 0.1 | 230.6 | 243.2 | 311.9 | 628.2 |
| | **227** | **238** | **305** | **634** |

one case: $Re = 200$, $k = 0.9$. This is presumably due to the fact that our analysis is limited to low-order (parabolic) radial variation in the fluid variables, whereas the FEA takes all higher-order terms into account. However, the 1D is much easier to implement and requires less time to run.

Next, we perform similar calculations as above, but this time we impose a sinusoidal variation of surface tension along the length of the microthread. This gives rise to Marangoni instability, wherein a shear stress develops that acts in the tangential direction at the free-surface. This must be balanced by viscous forces, which give rise to Marangoni flow at the interface with fluid moving from regions of lower surface tension towards regions of higher surface tension. This flow causes the free-surface to deform, thereby creating surface curvature and a corresponding pressure gradient within the jet that perpetuates and amplifies the curvature and flow. This ultimately leads to breakup [13–15, 29].

The surface tension at a liquid–gas interface may be perturbed by various factors including variations in temperature or surfactant along the interface. Here, we do not specify how the surface tension is modulated; rather we simply impose a fixed sinusoidal variation in the surface tension of the form

$$\sigma(z) = \sigma_0 \left[ 1 - \beta \left( 1 - \cos\left( \frac{2\pi z}{\lambda} \right) \right) \right], \tag{33}$$

where $\sigma_0$ is the surface tension at ambient temperature. We choose a peak-to-peak variation in $\sigma$ of approximately 1%, i.e. $\beta = 0.0048$.

We perform analysis for three different values of the Reynolds number, $Re = 1$, 10 and 100, and for each value we track the behavior of the free-surface to pinch-off for three different wavenumbers: $k = 0.45$, 0.7 and 0.9. The free-surface shapes for several of these cases at different times are shown in Figures 5 and 6. The computational grids for the three values of $k$ consisted of 205, 135 and 105 nodes, respectively, and the analysis took 4 s for the highest wavenumber and 16 s for the lowest wavenumber. These grid densities were established by successively increasing the number of nodes until the break-up times reached a steady state; it should be noted that for grid densities half of those previously mentioned, the break-up times only differed by 0.5%. In order to validate the model we repeat the analysis above using axisymmetric VOF CFD, which is performed using a commercial program, FLOW-3D (www.flow3d.com). In the CFD models the jet radius is as above, $r_0 = 100 \, \mu m$, and we use a uniform computational mesh with 2 $\mu m$ cell spacing in both the $r$ and $z$ directions. No significant changes were observed with a finer mesh. We compare the free-surface plots at pinch-off for the $Re = 100$ cases in Figure 7. The computational time for these cases ranged from 12 000 to 15 000 s, four orders of magnitude longer than the 1D analysis. The CFD free-surface profiles are somewhat different than the 1D analysis, especially for the shortest wavelength case, $k = 0.9$. Presumably this is due to radial dependencies that we ignore. Nevertheless, we obtain excellent agreement with the scaled time to pinch-off for both cases, as shown in Table II. Also, as noted above, while it is easy to impose initial perturbations to a microthread of fluid in our model, it can be very difficult to impose similar perturbations, especially infinitesimal free-surface displacements, using commercial VOF CFD programs. Table III gives

Re = 100, wavenumber = 0.45    Re = 100, wavenumber = 0.7    Re = 100, wavenumber = 0.9
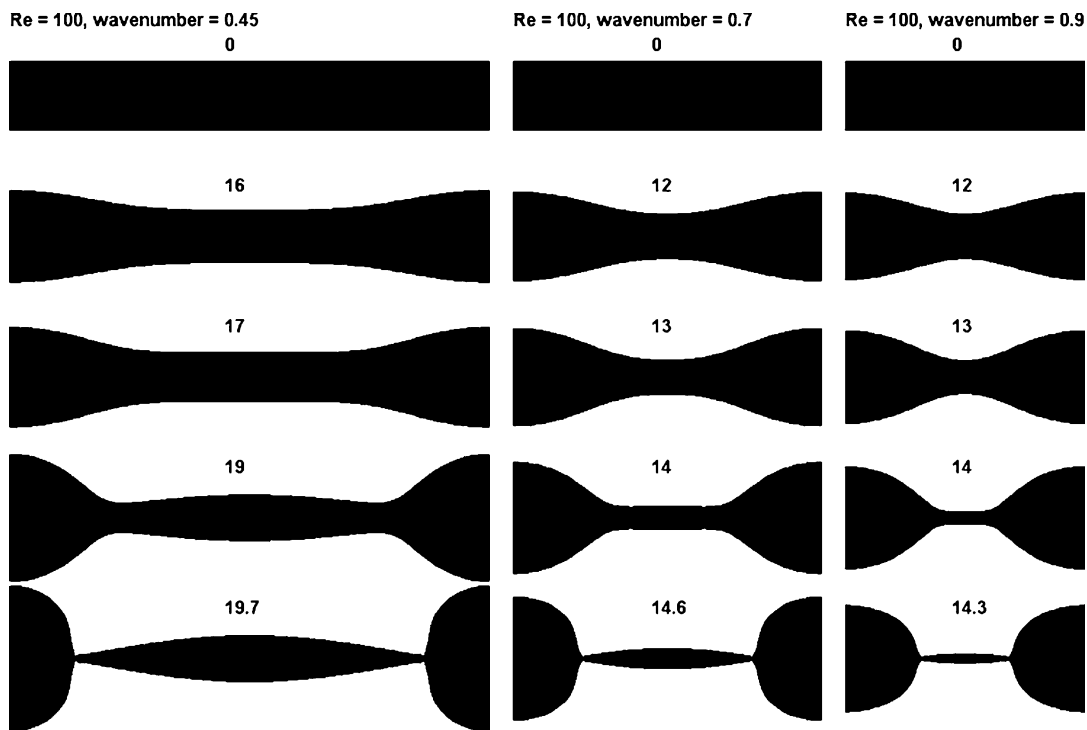
Figure 5. The shape of the free-surface as a function of scaled time ($t^* = t/t_c$) for $Re = 100$: Wavenumbers (from left): $k = 0.45$, $k = 0.7$ and $k = 0.9$.

Re = 1, wavenumber = 0.45    Re = 1, wavenumber = 0.7    Re = 1, wavenumber = 0.9
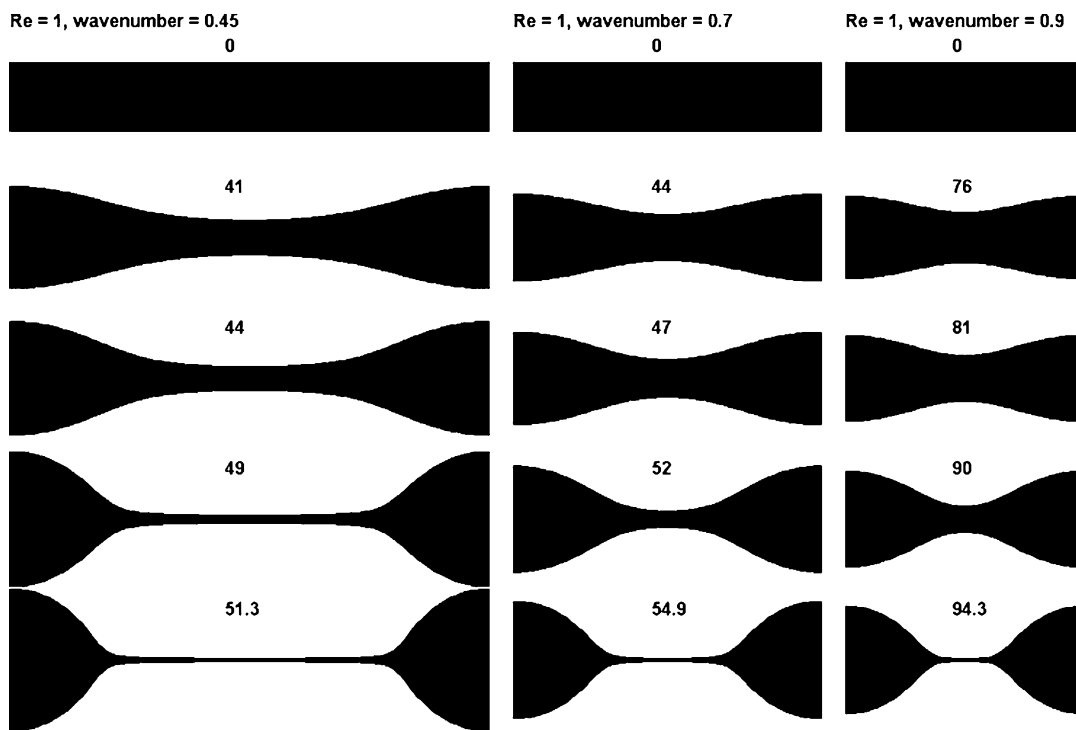
Figure 6. The shape of the free-surface as a function of scaled time ($t^* = t/t_c$) for $Re = 1$: Wavenumbers (from left): $k = 0.45$, $k = 0.7$ and $k = 0.9$.
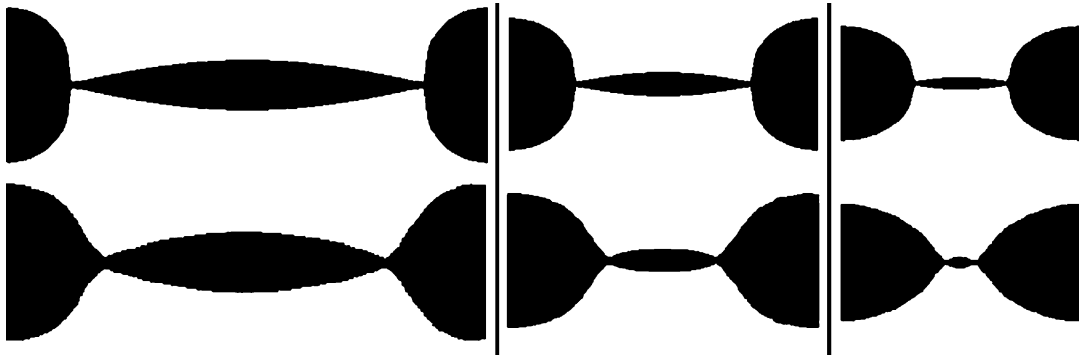
Figure 7. The shape of the free surface at pinch-off is shown for the 1D model (top row) compared with an axisymmetric CFD simulation (bottom row) for $Re = 100$. Wavenumbers are (from left) $k = 0.45$, 0.7, and 0.9.

Table II. A comparison of the scaled time to pinch-off from our model (bold-face) with an axisymmetric VOF CFD simulation (regular font).

| Reynolds Number | Wavenumber | | |
|---|---|---|---|
| | 0.45 | 0.7 | 0.9 |
| 100 | 21.12 | 15.6 | 15.57 |
| | **19.7** | **14.6** | **14.3** |
| 10 | 22.96 | 17.92 | 20.48 |
| | **25.5** | **17.3** | **19.2** |

Table III. A comparison of main drop and satellite volumes from our model (bold-face) with an axisymmetric CFD model is presented for the example presented in Figure 7.

| Volume (nL) | Wavenumber | | |
|---|---|---|---|
| | 0.45 | 0.7 | 0.9 |
| Main | 39.2 | 27.94 | 21.93 |
| | **38.17** | **27.48** | **21.66** |
| Satellite | 4.7 | 0.26 | 0.006 |
| | **5.44** | **0.49** | **0.06** |

the drop and satellite volumes in nanoLiters for the cases presented in Figure 7. To determine the drop volumes for the 1D model, we numerically integrated the free surface using the disk method. The CFD code reported the satellite drop volumes directly. Note that the 1D model predictions are more accurate at longer wavelengths, but less so at shorter wavelengths. This is presumably due to limitations of the low order radial variation that is assumed for the fluid behavior in the slender-jet analysis.

The various linear theories of jet break-up predict that the break-up time has a logarithmic dependence on the initial perturbation amplitude. The 1D model with surface tension perturbation possesses the same dependence as shown in Figure 8 [13]. The breakup time versus wavenumber for several different Reynolds numbers is presented in Figure 9. The minimum breakup time shifts to lower wavenumbers as the Reynolds number decreases (increasing viscosity). Also in Figure 9, we plot the wavenumber at the maximum growth rate ($k_{MGR}$) versus the Reynolds number. At low Reynolds number this plot reveals a near-logartihmic dependence. However, beyond a Reynolds number of about 20, $k_{MGR}$ levels out.
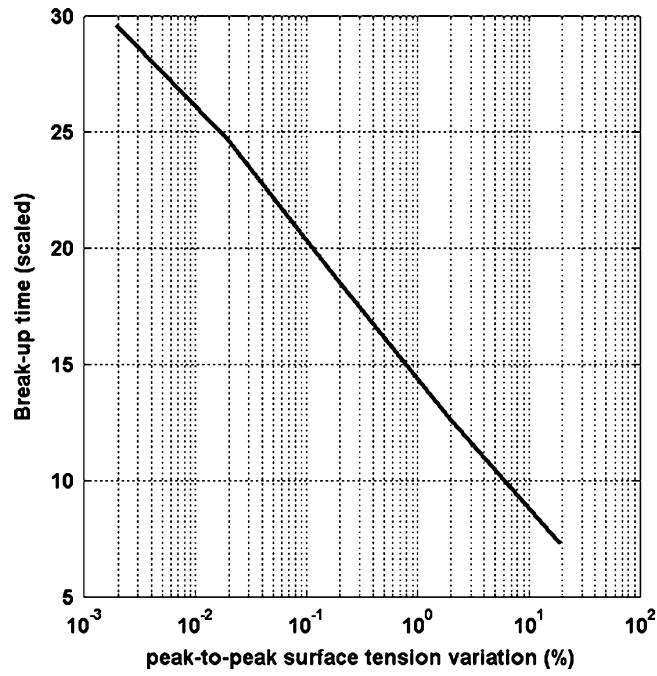
Figure 8. Scaled break-up time versus peak-to-peak surface tension variation for $Re=100$ and $k=0.7$.
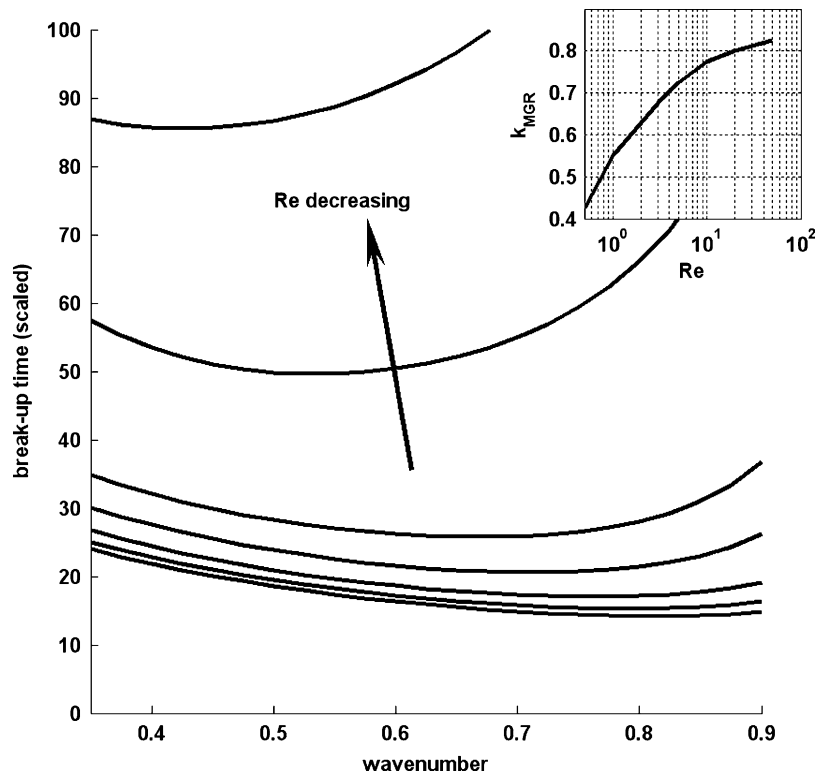


Figure 9. A plot of the break-up time versus wavenumber for $Re=50, 20, 10, 5, 3, 1, 0.5$. The inset shows the wavenumber at the maximum growth rate, $k_{MGR}$, versus Reynolds number.
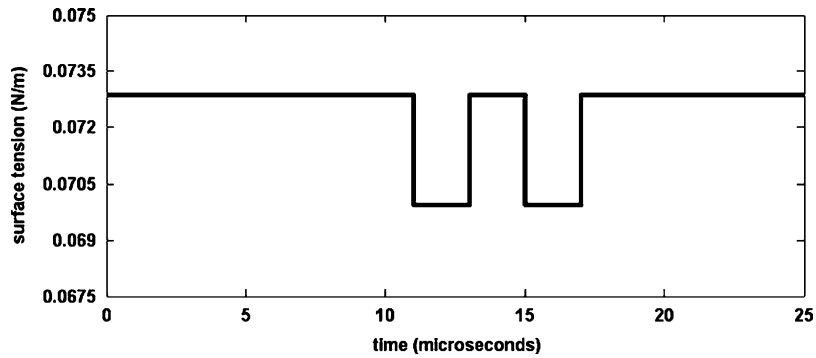
Figure 10. Surface tension at the orifice versus time for the nozzle-driven jet.
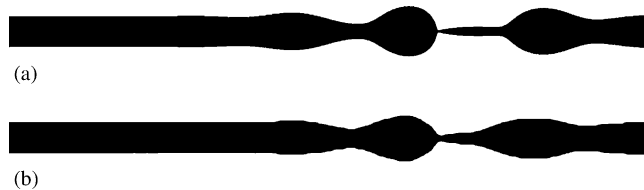


Figure 11. Predicted jet profile at pinch-off for the nozzle-driven jet: (a) 1D analysis and (b) VOF CFD.

Lastly, we apply our model to a continuous nozzle-driven microjet. We model a continuous jet of water with a radius of $r_0 = 5\,\mu m$ and a velocity of $10\,m/s$. For our 1D analysis, we define the computational domain from $z = 0$ (the orifice) to $z = 315\,\mu m$ and use 1050 uniformly spaced grid points. An inflow BC is imposed at the orifice ($z = 0$), and an outflow BC is imposed downstream, at the opposite end of the computational domain. The jet velocity is held constant at the orifice, and the surface-tension $\sigma$ is varied in a time-wise step fashion at this boundary, from a high of $0.073\,N/m$ to a low of $0.0696\,N/m$, as shown in Figure 10. The former value occurs at an ambient temperature of $20°C$, while the latter value can be achieved by heating the fluid to $40°C$. The time-dependent surface tension BCs mimics the time-dependent thermal stimulation used in the novel microfluidic drop generator discussed earlier and shown in Figure 1.

We use the 1D model to track the free-surface of the jet to pinch-off, and we compare this analysis with an axisymmetric VOF CFD simulation of the same system. In the CFD analysis, the computational domain spanned $0 \leqslant z \leqslant 250\,\mu m$, and we used a uniform mesh with a $0.2\,\mu m$ cell spacing in both the $r$ and $z$ directions. The jet profiles at pinch-off for the two models are compared in Figure 11. We found that the jet pinched-off in regions of lower surface tension, which is consistent with a linear theory of Marangoni instability developed by Furlani [13]. The time to pinch-off is predicted to be $28.0\,\mu s$ using the 1D model and $28.4\,\mu s$ using CFD, a difference of 1.4%. Also, the 1D analysis took approximately 5 min to complete, whereas the CFD simulation took 188 min on a comparable workstation, an increase of 380% in computational time. Furthermore, it is important to note that while it is easy to impose any arbitrary time-dependent modulation of the free-surface, velocity or surface tension at the orifice in our model, it can be very difficult to impose similar conditions in a commercial VOF CFD program.

## 4. CONCLUSIONS

We have developed a numerical model for predicting the instability and breakup of infinite microthreads and continuous nozzle-driven microjets of Newtonian fluid. The model is based on a slender-jet approximation, and has been implemented using the MOL numerical technique. We have used explicit time stepping and a uniform spatial grid, which are relatively easy to implement as

compared with other numerical techniques. The model takes into account arbitrary free-surface and velocity perturbations as well as Marangoni instability via variations in surface tension. We have validated the model using established data from the literature as well as VOF CFD simulations. The model enables jet instability predictions that are orders of magnitude faster than axisymmetric VOF CFD simulations. Furthermore, while it is easy to impose arbitrary free-surface, velocity and/or surface tension perturbations (modulation) in our model, similar conditions can be very difficult to implement in the commercial CFD software. The model is well suited for parametric analysis of jet breakup and satellite formation as a function of jet dimensions, modulation parameters and fluid rheology. It should be useful for the development and optimization of novel microfluidic droplet generators.

## REFERENCES

1. Savart F. Mémoire sur la constitution des veines liquides lancées par des orifices circulaires en mince paroi. *Annali di Chimica* 1833; **53**:337–386.
2. Plateau JAF. Sur les figures d'equilibre d'une masse liquide sans pesanteur. *Bruxelles Acad. Sci. Memoires* 1849 **23**:5.
3. Rayleigh L. On the capillary phenomena of jets. *Proceedings of the London Mathematical Society* 1879; **10**:4–13.
4. Ashgriz N, Mashayek F. Temporal analysis of capillary jet breakup. *Journal of Fluid Mechanics* 1995; **291**:163.
5. Eggers J, Villermaux E. Physics of liquid jets. *Reports on Progress in Physics* 2008; **71**:036601.
6. Ashley CT. Emerging applications for inkjet technology. *International Conference on Digital Printing Technologies*, San Diego, CA, vol. 18, 2002; 540–542.
7. Basaran OA. Small-scale free surface flows with breakup: drop formation and emerging applications. *AIChE Journal* 2002; **48**(9):1842–1848.
8. Sirringhaus H, Shimoda T. Inkjet printing of functional materials. *MRS Bulletin* 2003; **28**(11):802–803.
9. Tekin E, Smith PJ, Schubert US. Inkjet printing as a deposition and patterning tool for polymers and inorganic particles. *Soft Matter* 2008; **4**(4):703–713.
10. Roth EA, Xu T, Das M, Gregory C, Hickman JJ, Boland T. Inkjet printing for high-throughput cell patterning. *Biomaterials* 2004; **25**:3707–3715.
11. Calvert P. Inkjet printing for materials and devices. *Chemistry of Materials* 2001; **13**:3299–3305.
12. Chwalek JM, Trauernicht DP, Delametter CN, Sharma R, Jeanmaire DL, Anagnostopoulos CN, Hawkins GA, Ambravaneswaran B, Panditaratne JC, Basaran OA. A new method for deflecting liquid microjets. *Physics of Fluids* 2002; **14**(6):37–40.
13. Furlani EP. Temporal instability of viscous liquid microjets with spatially varying surface tension. *Journal of Physics A*: *Mathematical and General* 2005; **38**:263–276.
14. Furlani EP. Thermal modulation and instability of viscous microjets. *Proceedings of the NSTI Nanotechnology Conference*, Anaheim, CA, 2005.
15. Furlani EP, Price BG, Hawkins G, Lopez AG. Thermally induced Marangoni instability of liquid microjets with application to continuous inkjet printing. *Proceedings of the NSTI Nanotechnology Conference*, Boston, MA, 2006.
16. Scardovelli R, Zaleski S. Direct numerical simulation of free-surface and interfacial flow. *Annual Review of Fluid Mechanics* 1999; **31**:567–603.
17. Maronnier V, Picasso M, Rappaz J. Numerical simulation of free surface flows. *Journal of Computational Physics* 1999; **155**:439–455.
18. Sellens RW. A One-dimensional numerical model of the capillary instability. *Atomization and Sprays* 1992; **2**(4):239–251.
19. Lundgren TS, Mansour NN. Oscillations of drops in zero gravity with weak viscous effect. *Journal of Fluid Mechanics* 1988; **194**:479–510.
20. Hilbing JH, Heister SD. Droplet size control in liquid jet breakup. *Physics of Fluids* 1996; **8**:1574–1581.
21. Setiawan ER, Heister SD. Nonlinear modeling of an infinite electrified jet. *Journal of Electrostatics* 1997; **42**:243–257.
22. Hirt CW, Nichols BD. VOF method for the dynamics of free boundaries. *Journal of Computational Physics* 1981; **39**:201.
23. Sethian JA. *Level Set Methods*, *Cambridge Monographs on Applied and Computational Mathematics*. Cambridge University Press: Cambridge, U.K., 1996.

24. Anderson DM, McFadden GB, Wheeler AA. Diffuse interface methods in fluid mechanics. *Annual Review of Fluid Mechanics* 1998; **30**:139–165.
25. Eggers J, Dupont TF. Drop formation in a one-dimensional approximation of the Navier–Stokes equation. *Journal of Fluid Mechanics* 1994; **262**:205.
26. Brenner MP, Eggers J, Joseph K, Nagel SR, Shi XD. Breakdown of scaling in droplet fission at high Reynolds number. *Physics of Fluids* 1997; **9**:1573.
27. Ambravaneswaran B, Wilkes ED, Basaran OA. Drop formation from a capillary tube: comparison of one-dimensional and two-dimensional analyses and occurrence of satellite drops. *Physics of Fluids* 2002; **14**(8): 2606–2621.
28. Schiesser WE. *The Numerical Method of Lines Integration of Partial Differential Equations*. Academic Press: San Diego, 1991.
29. Gao Z. Instability of non-Newtonian jets with surface tension gradient. *Journal of Physics A*: *Mathematical and Theoretical* 2009; **42**:065501.